scientific reports

OPEN

Coherent control of anisotropic SPPs in a symmetric double-layer metal/uniaxial dielectric structure

Jabir Khan[1], Amjad Sohail[2], Amsyar Rahim[3], Muhammad Shafiq[1], Hazrat Ali[1]✉ & Saeed Haddadi[4]✉

We investigate the coherent control of anisotropic surface plasmon polaritons (SPPs) in a symmetric double-layer metal/uniaxial dielectric structure. The directional anisotropy introduced by the uniaxial dielectric enables tunable SPP dispersion, absorption, and propagation characteristics through an external control field. We analyze reflection and transmission spectra, dispersion relations, propagation lengths, and the scattering matrix eigenmodes. Our results reveal strong modulation of SPP wavelength and enhanced propagation length with varying control field strength and metal layer composition. Remarkably, we observe coherent perfect absorption for both symmetric and anti-symmetric modes, an effect not commonly realized in such layered anisotropic systems. This work introduces a novel platform for actively tunable nanoplasmonic devices, with potential applications in waveguiding, sensing, and plasmonic circuitry.

Keywords Surface plasmon polaritons, Reflection and transmission, Metal/uniaxial dielectric, Dispersion and absorption

Over the last several decades, plasmonics has developed rapidly, revealing the remarkable potential of surface plasmon polaritons (SPPs). SPPs are surface electromagnetic (EM) waves that arise through the coupling of incident EM radiation with the collective charge-density oscillations of free electrons in a metal[1–3]. The persistence of SPPs by metallic structures is a fascinating method for applications in biosensing[4], plasmonic-based solar cells[5], subwavelength aperture transmission[6,7], and photodetectors[8]. These applications typically exploit the strong field enhancement and surface confinement normal to the interface provided by propagating SPPs, as well as their high sensitivity to changes in the surrounding dielectric environment[9,10]. Although propagating SPPs provide strong EM field confinement perpendicular to the metal/dielectric interface and significant field enhancement near the surface, their in-plane wavelength remains only slightly shorter than the free-space wavelength. This distinguishes them from deeply subwavelength phenomena such as localized surface plasmon resonances (LSPRs) or spoof SPPs, which exhibit stronger spatial confinement in all directions[1].

To achieve more accurate characterization of isotropic SPPs, some researchers have employed various methodologies and models[11–13]. Consequently, graphene-based 2D heterostructures[14], 3D hybrid systems[15], thin-layer and double-layer interfaces of isotropic dielectrics have been studied for unique SPP configurations, dispersion/absorption spectra, control over scattering, and loss mitigation. Similarly, metallic double layer structures in isotropic media have been used to enhance propagation length, analyze different EM eigenmodes, and investigate the nonlinear interactions of SPPs[16–19].

The study of SPPs in anisotropic media has attracted increasing attention due to additional degrees of freedom in controlling light–matter interaction, which are absent in isotropic media[20–23]. The anisotropic SPPs arise at the interface between a metal and an anisotropic dielectric (typically uniaxial), where direction-dependent permittivity leads to propagation characteristics that differ from those of conventional (isotropic) SPPs. This anisotropy affects the dispersion, confinement, and loss properties of the SPP modes, making them highly tunable and suitable for coherent control and waveguiding applications. Anisotropic materials have the advantage that their dielectric properties depend on direction[24–26]. In this context, SPPs have been investigated using anisotropic/bi-anisotropic substrates[25,27], lossy uniaxial materials[28], semiconductor inclusions[29], nanowire metamaterials[30], nanocomposites[31], and 2D materials[32]. Similarly, uniaxial SPPs[33] and biaxial[34] media offer

[1]Department of Physics, Abbottabad University of Science and Technology, Havellian 22500, Pakistan. [2]Department of Physics, Government College University, Allama Iqbal Road, Faisalabad 38000, Pakistan. [3]Department of Physics, Faculty of Science Universiti Putra Malaysia, Serdang, Selangor 43400, Malaysia. [4]School of Particles and Accelerators, Institute for Research in Fundamental Sciences (IPM), P.O. Box 19395–5531, Tehran, Iran. ✉email: yamanuom@gmail.com; haddadi@ipm.ir

various tools to manipulate EM waves at the nanoscale, in contrast to isotropic media. In such manipulation, the complex dispersion relation of SPPs, their wavelength, propagation length, optical axis orientation, permittivity tensors, and polarization states play vital roles and enable precise control over SPP's behavior[34–36].

The dispersion relations of SPPs in anisotropic layers, especially in double-layer systems, depend on the anisotropic properties of the materials comprising the layers[37,38]. The optical axis in anisotropic dielectrics enhances both the confinement and propagation length of SPPs in configurations such as graphene double layers[39–42]. The anisotropic double-layer system allows SPPs to probe the relative permittivity tensors of each layer, thereby influencing propagation and inducing birefringence, through which SPP modes split based on their polarization directions. The coupling of the plasmon mode between two layers affects the total energy transfer and propagation length, while offering tunable characteristics. Anisotropic materials enable the adjustment of surface plasmon resonance conditions, thus enhancing the system's sensitivity to polarization states. These anisotropic materials provide an accurate platform for anisotropic analysis, and the application of SPPs in double-layer structures opens new horizons in fundamental research[36,40,43,44].

Contribution and motivation

SPPs at metal/dielectric interfaces have been extensively investigated due to their ability to confine EM energy at subwavelength scales. However, most studies focus on isotropic dielectric environments, where the in-plane propagation characteristics are uniform. In contrast, our work considers SPPs at interfaces involving *uniaxial anisotropic dielectrics*, where the permittivity tensor features distinct components along the ordinary and extraordinary axes. This anisotropy modifies the dispersion relation and field confinement, resulting in direction-dependent SPP behavior. The anisotropic nature enables enhanced control of the SPP wavelength, propagation length, and absorption via external fields. Such configurations are gaining attention for their potential in tunable plasmonic devices, waveguides, and sensing platforms, but remain less explored compared to their isotropic counterparts.

Considering the above literature, we observe that no study has yet been reported on the coherent control of anisotropic SPPs in a symmetric double-layer metal/uniaxial dielectric structure. Therefore, in this article, we study the coherent control of anisotropic SPPs in a three-level Λ-type atomic configuration. We find that the wavelength of SPPs increases with increasing fractional ratios of the metallic components, f_1 and f_2, while the propagation length is enhanced by the control field Ω_c. The reflection, transmission, and symmetric and anti-symmetric eigenvalues of the scattering matrix are also modified by probe detuning (Δ_p), control field (Ω_c), and f_1, f_2. The results of this study may find significance in sensing, computing, and waveguiding technologies.

Innovation and organization

The novelty of our work lies in the combination of coherent control and anisotropic plasmonics within a symmetric double-layer metal/uniaxial dielectric interface. While prior studies have addressed SPP propagation in isotropic or single-interface systems, our model introduces a directionally tunable platform where both field-induced modulation and material anisotropy play a key role. Furthermore, we report coherent perfect absorption (CPA) in both symmetric and anti-symmetric modes of the scattering matrix;an effect that, to our knowledge, has not been demonstrated in such anisotropic layered systems. This approach provides a powerful mechanism for dynamically reconfiguring SPP characteristics, with implications for integrated plasmonic waveguiding and optical switching.

The paper is structured as follows: Section "Theory and model" presents the analytical formulation for SPPs propagating along the interfaces of the layered structure, which acts as a plasmonic waveguide. Section "Results and discussion" provides our results on dispersion and absorption spectra, wavelength, propagation distance, reflection and transmission spectra, and symmetric/anti-symmetric eigenmodes of the scattering matrix. Finally, in Section "Conclusions", we summarize our findings.

Theory and model

Let us consider a symmetric double-layer metal/uniaxial dielectric structure where the dielectric tensors of the first and second layers ($\epsilon_{1d}, \epsilon_{2d}$) respectively contain a three-level Λ-type atomic configuration. As shown in Fig. 1, $\epsilon^{\perp}_{1,2}$ and $\epsilon^{\|}_{1,2}$ are the normal and parallel permittivity components of the anisotropic materials in both layers. The permittivity tensor $\bar{\epsilon}_{(1,2)}$ of the uniaxial dielectric medium in both layers is given as:

$$\bar{\epsilon}_{(1,2)} = \begin{bmatrix} \epsilon^{\perp}_{(1,2)} & 0 & 0 \\ 0 & \epsilon^{\perp}_{(1,2)} & 0 \\ 0 & 0 & \epsilon^{\|}_{(1,2)} \end{bmatrix}, \tag{1}$$

where $\epsilon^{\perp}_{(1,2)}$ and $\epsilon^{\|}_{(1,2)}$ are the effective permittivity components normal and parallel to the optical axis, respectively, for both layers. Note that we assume that the uniaxial dielectric medium has its optical axis aligned along the z-direction, leading to a diagonal permittivity tensor of the form $\bar{\epsilon}_{(1,2)}$. This model is appropriate for aligned, non-gyrotropic uniaxial crystals and neglects magneto-optical or chiral effects that would introduce off-diagonal tensor elements. The inclusion of such off-diagonal terms would modify the SPP dispersion by coupling transverse field components and possibly breaking reciprocity, which is an important extension we plan to consider in future work. These effective permittivities are obtained using the mixing formula for layered characteristics[45]:

$$\epsilon^{\perp}_{j} = f_j \epsilon^{m}_{j} + (1 - f_j)\epsilon_{jd} \tag{2}$$

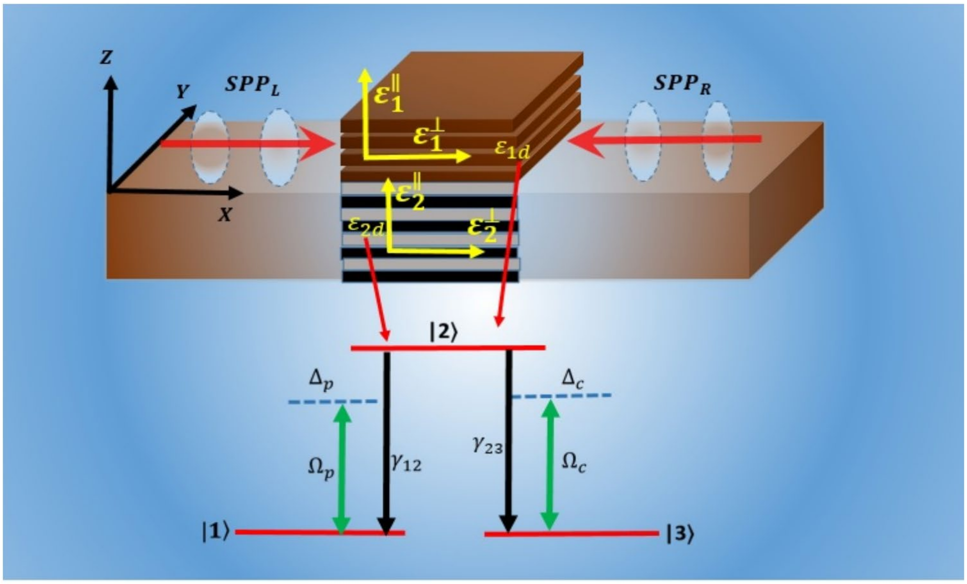

Figure 1. The diagram of a symmetric double-layer metal/uniaxial dielectric structure with a three-level Λ -type atomic configuration, where SPP_L and SPP_R impinge on the first layer from the left and right.

and

$$\epsilon_j^{\parallel} = \frac{1}{\frac{f_j}{\epsilon_j^m} - \frac{(1-f_j)}{\epsilon_{jd}}}, \tag{3}$$

in which $j = 1, 2$, and by the Drude model, $\epsilon_j^m = \left(1 - \frac{\omega_p^2}{\omega^2 + i\omega\Gamma}\right)$, where $\omega = 3.6 \times 10^{15}$, $\omega_p = 1.5 \times 10^{16}$ is the plasma frequency, and $\Gamma = 138.7 \times 10^{13}$ is the damping rate.

Our model consists of $|1\rangle$ and $|3\rangle$ as ground states, while $|2\rangle$ is an upper excited state. The probe laser pulse Ω_p and the control field Ω_c, with Rabi frequencies Ω_p and Ω_c, couple the transitions $|2\rangle \Longleftrightarrow |1\rangle$ and $|2\rangle \Longleftrightarrow |3\rangle$, respectively, with decay rates γ_{12} and γ_{23} (see Fig. 1). The interaction Hamiltonian of this system is

$$H = -\frac{\hbar}{2}[\Omega_p e^{-i\Delta_p t}|2\rangle\langle 1| + \Omega_c e^{-i\Delta_c t}|2\rangle\langle 3|] + \text{H.c.} \tag{4}$$

Here, Δ_p and Δ_c are the probe and control field detunings. By using the rotating-wave approximation, the evolution of the density operator ρ is given as:

$$\dot{\rho} = \frac{[H, \rho]}{i\hbar} - \Gamma\rho. \tag{5}$$

We use the rotating-wave approximation and the interaction Hamiltonian to derive the density matrix elements for the three-level Λ-type configuration, which are obtained as:

$$\begin{aligned}
\dot{\rho}_{11} &= (\rho_{33}-\rho_{11})\gamma_{31}+\gamma_{21}\rho_{22}-\frac{i}{2}\Omega_p(\rho_{21}-\rho_{12}),\\
\dot{\rho}_{12} &= \rho_{12}(-\gamma_{12}-i\Delta_p)+\frac{i}{2}\Omega_p(\rho_{22}-\rho_{11})-\frac{i}{2}\Omega_c\rho_{13},\\
\dot{\rho}_{21} &= \rho_{21}(i\Delta_p-\gamma_{21})+\frac{i}{2}\Omega_p(\rho_{11}-\rho_{22})+\frac{i}{2}\Omega_c\rho_{31},\\
\dot{\rho}_{22} &= -\rho_{22}(\gamma_{23}+\gamma_{21})+\frac{i}{2}\Omega_p(\rho_{12}-\rho_{21})-\frac{i}{2}\Omega_c(\rho_{32}-\rho_{23}),\\
\dot{\rho}_{23} &= \rho_{23}(i\Delta_c-\gamma_{23})+\frac{i}{2}\Omega_p\rho_{13}+\frac{i}{2}\Omega_c(\rho_{33}-\rho_{22}),\\
\dot{\rho}_{32} &= -\rho_{32}(i\Delta_c+\gamma_{32})+\frac{i}{2}\Omega_c(\rho_{22}-\rho_{33})-\frac{i}{2}\Omega_p\rho_{31},\\
\dot{\rho}_{33} &= (\rho_{11}-\rho_{33})\gamma_{31}+\gamma_{23}\rho_{22}+\frac{i}{2}\Omega_c(\rho_{23}-\rho_{32}),\\
\dot{\rho}_{13} &= -\rho_{13}(\gamma_{13}+i(\Delta_p-\Delta_c))+\frac{i}{2}\Omega_p\rho_{23}-\frac{i}{2}\Omega_c\rho_{12},\\
\dot{\rho}_{31} &= -\rho_{31}(\gamma_{31}+i(\Delta_c-\Delta_p))+\frac{i}{2}\Omega_c\rho_{21}-\frac{i}{2}\Omega_p\rho_{32}.
\end{aligned} \tag{6}$$

For the density matrix elements at the steady state, we get:

$$\rho_{21} = \frac{i(\gamma_{31}+(\Delta_p-\Delta_c))\Omega_p}{(\gamma_{21}\gamma_{31}+i\gamma_{21}\Delta_c-i\gamma_{21}\Delta_p-i\gamma_{31}\Delta_p+\Delta_p\Delta_c-\Delta_p^2\Omega_c^2)}. \tag{7}$$

Note that we focus on the steady-state regime, which assumes that the system reaches a time-independent density matrix when driven by continuous-wave (CW) or quasi-CW fields. This is a valid approach when the pulse duration of the SPP excitation is much longer than the coherence times of the atomic transitions involved in the three-level Λ-system. For typical atomic media under weak probe and moderate control fields, the coherence time is on the order of microseconds to nanoseconds, while the relevant SPP propagation time across the structure is several picoseconds to nanoseconds. Therefore, for excitation with pulses significantly longer than the coherence time (e.g., CW or nanosecond pulses), the adiabatic approximation holds well and the steady-state solution is justified.

The dielectric tensors of the two uniaxial dielectric layers, denoted by ϵ_{1d} and ϵ_{2d}, are described by

$$\epsilon_{1d} = \epsilon_{2d} = 1+\chi, \tag{8}$$

here $\chi = \eta\rho_{21}$ with $\eta = \frac{N|\mu_{21}|}{\epsilon_0\hbar\Omega_p}$ where μ_{21} is the atomic dipole matrix element and N is the atomic number density. The dielectric constant in terms of coherence term ρ_{21} is obtained by:

$$\epsilon_{1d} = \epsilon_{2d} = 1+\eta\rho_{21}. \tag{9}$$

By using Maxwell's equations, $\nabla\times \mathrm{B} = \epsilon_r\epsilon_0\frac{\partial \mathrm{E}}{\partial t}$ and $\nabla\times\mathrm{E} = -\mu_0\frac{\partial \mathrm{B}}{\partial t}$, and the analytical formula for SPPs propagating in an external waveguide with a wave vector $k = (k_x, 0, k_z)$, the longitudinal and perpendicular components are given by:

$$k_x = \frac{\omega}{c}\sqrt{\frac{\epsilon_1\epsilon_2}{\epsilon_1+\epsilon_2}}, \quad k_z^{(1,2)} = \sqrt{\epsilon_{(1,2)}\frac{\omega^2}{c^2}-k_x^2}. \tag{10}$$

For the case of an interface between two uniaxial materials, for wave vector $K = (K_x, 0, K_z)$, a complex dispersion relation is given as:

$$K_x = \frac{\omega}{c}\sqrt{\frac{\epsilon_1^{\|}\epsilon_2^{\|}\left(\epsilon_1^{\perp}-\epsilon_2^{\perp}\right)}{\epsilon_1^{\perp}\epsilon_1^{\|}-\epsilon_2^{\perp}\epsilon_2^{\|}}}, \tag{11}$$

$$K_z = \sqrt{\epsilon_{1,2}^{\perp}\left(\frac{\omega^2}{c^2}-\frac{K_x^2}{\epsilon_{1,2}^{\|}}\right)}. \tag{12}$$

Furthermore, the wavelength (λ_{sppx}) and propagation length (L_{sppx}) are determined by:

$$\lambda_{\mathrm{sppx}} = \frac{2\pi}{\mathrm{Re}[K_x]} \tag{13}$$

and

$$L_{\mathrm{sppx}} = \frac{1}{\mathrm{Im}[K_x]}. \tag{14}$$

Let the SPPs propagate in the z-direction ($K_z = k_z$), then the following equalities can be written as[46]:

$$\frac{\epsilon_1^{\perp}}{\epsilon_2^{\perp}} = \frac{\epsilon_1}{\epsilon_2}, \quad \frac{\epsilon_1^{\parallel}}{\epsilon_2^{\parallel}} = \frac{\epsilon_1}{\epsilon_2}. \tag{15}$$

Now, the amplitudes of the plasmons that are transmitted and reflected at the interface of the metal/uniaxial dielectric layers of finite length L are given by:

$$R = \frac{r(1 - e^{2iK_xL})}{1 - r^2 e^{2iK_xL}} \tag{16}$$

and

$$T = \frac{e^{iK_xL}(1 - r^2)}{1 - r^2 e^{2iK_xL}}. \tag{17}$$

Here, r and t are given by the Fresnel formulas for a plane wave incident on the interface:

$$r = \frac{\frac{k_x}{\epsilon_2} - \frac{K_x}{\epsilon_2^{\parallel}}}{\frac{k_x}{\epsilon_2} + \frac{K_x}{\epsilon_2^{\parallel}}}, \quad t = \frac{\frac{2k_x}{\epsilon_2}}{\frac{k_x}{\epsilon_2} + \frac{K_x}{\epsilon_2^{\parallel}}}. \tag{18}$$

When the system is illuminated from both sides, the scattering matrix relates the left (S_l) and right (S_r) input and output amplitudes as follows:

$$\begin{bmatrix} S_r^{\mathrm{out}} \\ S_l^{\mathrm{out}} \end{bmatrix} = \bar{S} \begin{bmatrix} S_r^{\mathrm{in}} \\ S_l^{\mathrm{in}} \end{bmatrix}, \tag{19}$$

where

$$\bar{S} = \begin{bmatrix} R & T \\ T & R \end{bmatrix}. \tag{20}$$

Finally, $S_{\pm}$ (with + for symmetric and – for anti-symmetric modes) are the eigenmodes of the slab structure, and the eigenvalues of the scattering matrix are given by[47,48]:

$$S_{\pm} = R \pm T = 0. \tag{21}$$

Results and discussion

This section contains our outcomes. We find the dispersion relation of SPPs, wavelength, propagation length, and reflection and transmission coefficients (by using the scattering matrix) for a symmetric double-layer metal/uniaxial dielectric structure. A three-level Λ-type configuration is considered for anisotropic SPPs in the metal/uniaxial dielectric interfaces of both layers. The incident wavelength of the field is $\lambda = 2\pi c/\omega$, the decay rate γ is considered $2\pi \times 10^{12}$ Hz, and all other parameters are fixed as $\gamma_{21} = 0.5\gamma, \gamma_{31} = 0.0001\gamma, \omega = 3.6 \times 10^{15}$, $\omega_p = 1.5 \times 10^{16}$, $\mu_{21} = 8.478 \times 10^{-30}$, $N = 1 \times 10^{12}\ \mathrm{m}^{-3}$, and $\Gamma = 138.7 \times 10^{13}$.

Dispersion and absorption spectrum

In Fig. 2a, we plot the dispersion spectrum of SPPs versus probe detuning Δ_p for various control field strengths. As Ω_c increases, this causes strong polarization coupling between different eigenstates, which modifies the propagation characteristics of SPPs. We notice a normal slope around the resonance for $\Omega_c = 0.5\gamma, 1\gamma, 1.5\gamma$, leading to the slow propagation of SPPs. Furthermore, we see two anomalous dispersion curves at SPPs resonance (see the red curve Fig. 2a). By changing the value of the fraction ratio of metallic components of both layers (f_1, f_2), the dispersion spectra versus probe detuning are shown in Fig. 2b. We observe a normal slope around the resonance for $f_1 = 0.10; f_2 = 0.20$, $f_1 = 0.20; f_2 = 0.30$ and $f_1 = 0.30; f_2 = 0.40$, revealing the slow propagation of the SPPs (see Fig. 2b). The absorption spectrum of SPPs as a function of probe detuning with increasing values of Ω_c and f_1, f_2 is plotted in Fig. 2c,d. The absorption profile is influenced by strong control field coupling between different eigenstates. We notice that zero absorption around the resonance (shifted to $\Delta_p = 0.5\gamma$) reveals plasmon-induced transparency. Moreover, the width of the transparency window increases for $\Omega_c = 1\gamma$ and 1.5γ. For both the positive and negative regions of probe detuning, we observe two symmetrical absorption peaks; see Fig. 2c. Additionally, Fig. 2d demonstrates the absorption spectrum of SPPs versus Δ_p for various fraction ratios of metallic components of both layers. At the resonance point $\Delta_p = 0$, the absorption is zero. A gradual change in f_1 and f_2 raises the absorption spectrum, which is maximal at $f_1 = 0.30$ and $f_2 = 0.40$. We also observe two symmetrical absorption peaks at certain positive and negative values of probe detuning.

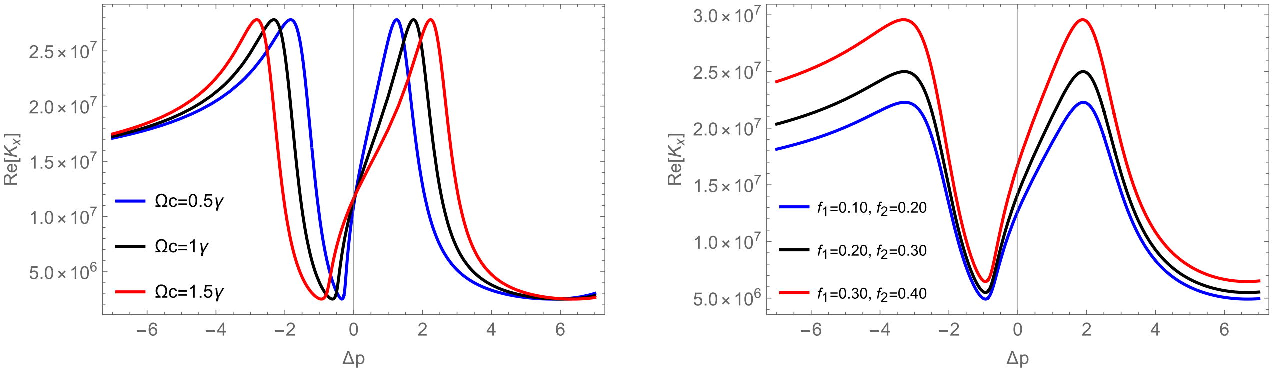

(a) Real part of K_x versus Δ_p for different values of Ω_c with $\Delta_c = 0\gamma$, $f_1 = 0.30$, and $f_2 = 0.70.$,$\gamma_{21} = 1\gamma$

(b) Real part of K_x versus Δ_p for different values of f_1 and f_2 with $\Delta_c = 0\gamma$ and $\Omega_c = 1.5\gamma$, $\gamma_{21} = 1\gamma$.

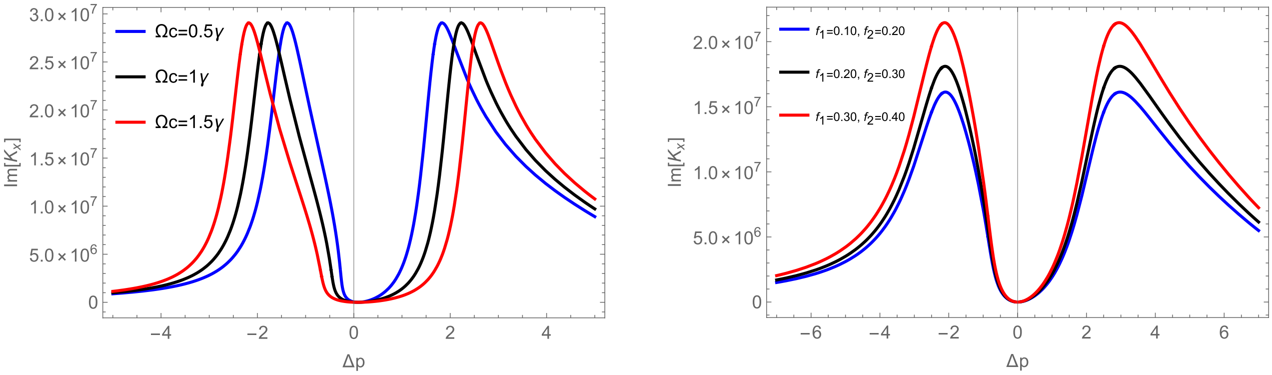

(c) Imaginary part of K_x versus Δ_p for different values of Ω_c with $\Delta_c = 0.09\gamma$, $f_1 = 0.10$, and $f_2 = 0.60$, $\gamma_{21} = 1\gamma$.

(d) Imaginary part of K_x versus Δ_p for different values of f_1 and f_2 with $\Delta_c = 0\gamma$ and $\Omega_c = 1.5\gamma$, $\gamma_{21} = 1.5\gamma$.

Figure 2. Dispersion and absorption spectrum of SPPs.

Wavelength

Figure 3 illustrates the wavelength spectrum of SPPs , which lie in the sub-wavelength regime. In Fig. 3a, we plot the wavelength of SPPs as a function of probe detuning for different control field strengths. We observe wavelengths of 470 nm for $\Omega_c = 1\gamma$ and 440 nm at the control field $\Omega_c = 1.5\gamma$ in the negative detuning region. On the positive detuning side at $\Delta_p = 0.15\gamma$, the wavelength is 560 nm. From $\Delta_p = 1\gamma$, the wavelength for $\Omega_c = 0.5\gamma, 1\gamma$ and 1.5γ is found to be 190 nm, 270 nm, and 80 nm, respectively (see blue, black, and red curves). Figure 3b shows the wavelength spectrum of SPPs versus Δ_p for different fraction ratios of metallic components of layer 1 (f_1) and layer 2 (f_2). By increasing f_1 and f_2, we observe that the wavelength increases from 370 nm up to 450 nm for negative values of Δ_p, and for positive values of detuning, λ_{sppx} increases from 120 nm to 200 nm. Moreover, Fig. 3c and d depict the wavelength spectrum of SPPs versus control field strength Ω_c for different probe detunings Δ_p and fraction ratios of metallic components. By increasing Δ_p, λ_{sppx} increases, and we observe wavelengths of 250 nm and 290 nm at probe detunings $\Delta_p = 0\gamma$ and $\Delta_p = 0.2\gamma$, while for $\Delta_p = 0.4\gamma$, we have $\lambda_{\text{sppx}} = 420$ nm. Similarly, increasing f_1 and f_2 enhances the wavelength spectrum from 195 nm up to 475 nm, as can be seen in Fig. 3d.

Propagation length

For the propagation length of SPPs, we plot L_{sppx} versus probe detuning for different strengths of the control field, as shown in Fig. 4a. When we increase Ω_c, the propagation distance of SPPs increases, and we observe $L_{\text{sppx}} = 180\mu$m, 310μm and 420μm for the respective control field strengths $\Omega_c = 0.5\gamma$, 1γ, and 1.5γ, as shown in Fig. 4a. For the fraction ratio of metallic components of both layers, f_1 and f_2, we notice that the propagation distance of SPPs is 640 μm at $f_1 = 0.10$, $f_2 = 0.20$, 380 μm for $f_1 = 0.20$, $f_2 = 0.30$, and 200 μm for $f_1 = 0.30$, $f_2 = 0.40$ (see Fig. 4b). In Fig. 4c,d, we plot L_{sppx} as a function of Ω_c for different probe detunings and values of f_1 and f_2. We find that increasing probe detuning values ($0\gamma, 0.2\gamma, 0.4\gamma$) enhances the propagation distance of SPPs up to 600 μm at distinct control field strengths (see blue, red, and black curves). Figure 4d shows L_{sppx} against Ω_c for various fraction ratios of metallic components of both layers. We notice $L_{\text{sppx}} = 360$ μm, 230 μm, and 140 μm for $f_1 = 0.10$, $f_2 = 0.20$, $f_1 = 0.20$, $f_2 = 0.30$, and $f_1 = 0.30$, $f_2 = 0.40$, respectively.

It is important to highlight the physical mechanisms responsible for the extended SPP propagation lengths reported in this work. In conventional isotropic metal/dielectric interfaces, the propagation length is typically limited to about 100 μm due to intrinsic Ohmic losses in the metal and absorptive losses in the dielectric[49]. In our structure, the introduction of a uniaxial dielectric with embedded three-level Λ-type atoms enables coherent

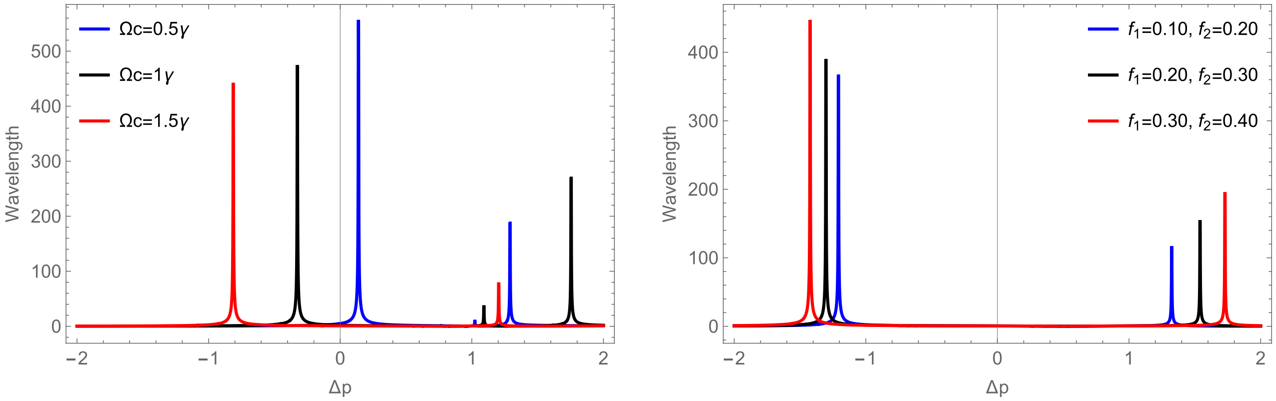

(a) Wavelength versus Δ_p for different values of Ω_c where $\Delta_c = 1\gamma$, $f_1 = 0.10$, and $f_2 = 0.20$.

(b) Wavelength versus Δ_p for different values of f_1 and f_2 where $\Delta_c = 1\gamma$ and $\Omega_c = 1.5\gamma$.

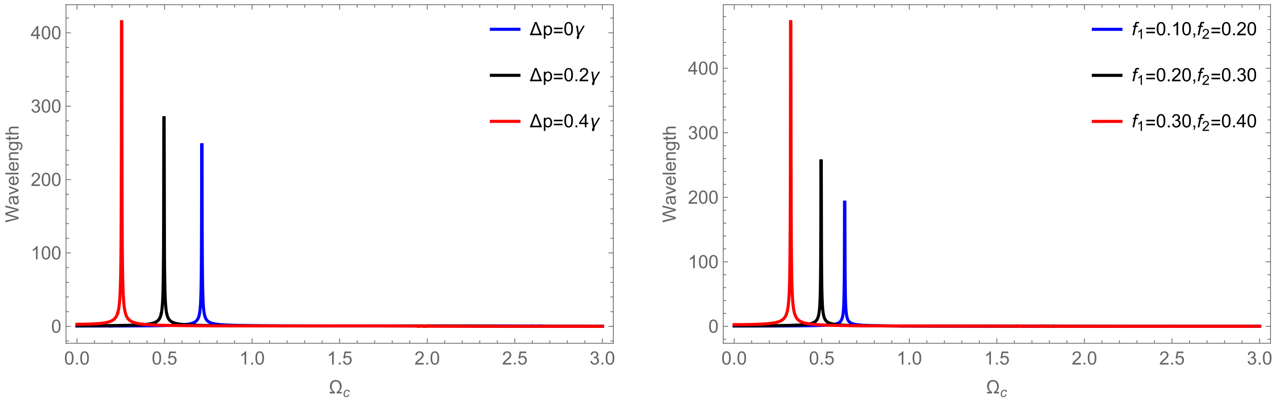

(c) Wavelength versus Ω_c for different values of Δ_p where $\Delta_c = 1\gamma$, $f_1 = 0.10$, and $f_2 = 0.20$.

(d) Wavelength versus Ω_c for different values of f_1 and f_2 where $\Delta_c = 1\gamma$ and $\Delta_p = 0\gamma$.

Figure 3. Wavelength of SPPs.

control of absorption through electromagnetically induced transparency (EIT)-like effects. By tuning the control field strength (Ω_c) and probe detuning (Δ_p), we suppress the imaginary part of the dielectric permittivity, thereby reducing absorption losses and extending the SPP propagation length significantly. Additionally, the engineered anisotropy further tailors the dispersion relation, enhancing mode confinement and minimizing radiative leakage. This demonstrates that the combination of coherent population trapping and anisotropic interface design provides an effective route for achieving long-range, low-loss SPP propagation, which is highly desirable for practical nanophotonic devices.

Reflection and transmission

In Fig. 5, with the help of Eqs. (16) and (17), we plot the reflection and transmission spectra for different control field strengths and fraction ratios of metallic components of both layers. Fig. 5a illustrates the reflection spectrum versus probe detuning for three values of Ω_c. On the negative detuning side, we see a sharp dip (indicating zero reflection) at $\Omega_c = 0.5\gamma$ (blue-solid curve), which becomes broader and shifts to $\Delta_p = -0.2\gamma$ (the red-solid curve) and -0.32γ (the green-solid curve) for $\Omega_c = 1\gamma$ and 1.5γ, respectively. At the resonance point, we observe 65% reflection, which then becomes partial (50%) on the positive probe detuning side (0.6γ, 0.85γ, 1.2γ), and reaches a maximum at $\Delta_p = 2\gamma$ for all respective values of the control field (see Fig. 5a).

For the transmission spectrum shown in Fig. 5b, as the control field increases, we observe peaks in the regime of negative detuning, which indicate complete transmission. At the resonance point, one can see 35% transmission. Beyond probe detuning $\Delta_p = 0\gamma$, the transmission spectrum gradually decreases, and at $\Delta_p = 1.3\gamma$ to 2γ, the transmission is zero for $\Omega_c = 0.5\gamma$, 1γ, and 1.5γ (see blue, red, and green curves).

Figure 5c,d illustrates the reflection and transmission spectra versus probe detuning for different fraction ratios (f_1, f_2) of metallic components. We observe reflection dips for $f_1 = 0.10$, $f_2 = 0.20$, $f_1 = 0.20$, $f_2 = 0.30$, and $f_1 = 0.30$, $f_2 = 0.40$ at $\Delta_p = -0.3\gamma$, -0.2γ, and -0.1γ, respectively. At a probe detuning of 0.2γ, we notice 80% reflection, and at $\Delta_p = 0.8\gamma$ we have 90% reflection for $f_1 = 0.30$, $f_2 = 0.40$, which then reaches a maximum at $\Delta_p = 2\gamma$ for all values of f_1 and f_2. Similarly, in Fig. 5d, we plot the transmission spectrum for various values of the fraction ratios of metallic components of both layers. We find maximum transmission on the negative side of probe detuning ($\Delta_p = -0.3\gamma$, -0.2γ, and -0.1γ) (blue, red, and green peaks), and minimum transmission occurs for $\Delta_p = 1.3\gamma$ to 2γ.

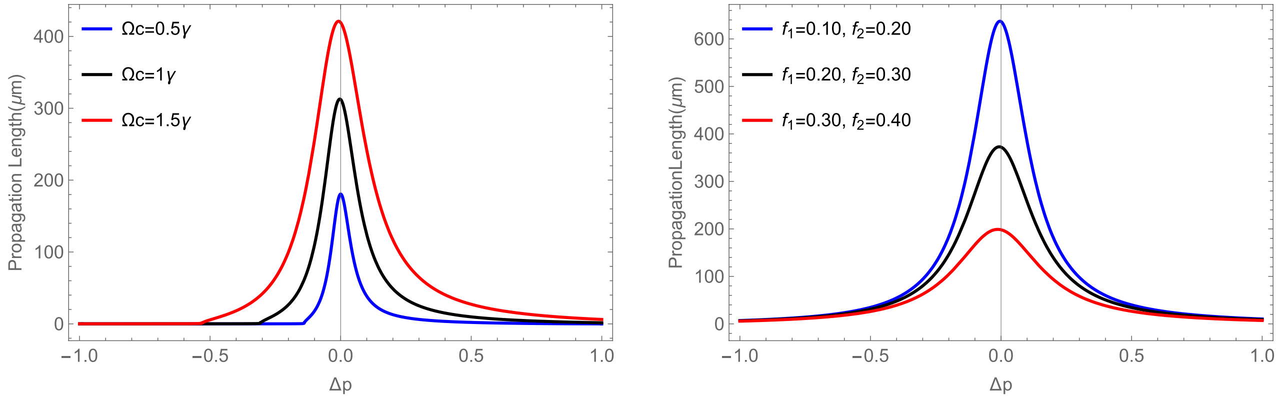

(a) Propagation length versus Δ_p for different values of Ω_c where $\Delta_c = 1\gamma$, $f_1 = 0.10$ and $f_2 = 0.20$, $\gamma_{21} = 0.06\gamma$.

(b) Propagation length versus Δ_p for different values of f_1 and f_2 where $\Delta_c = 0\gamma$ and $\Omega_c = 4\gamma$,$\gamma_{21} = 0.5\gamma$.

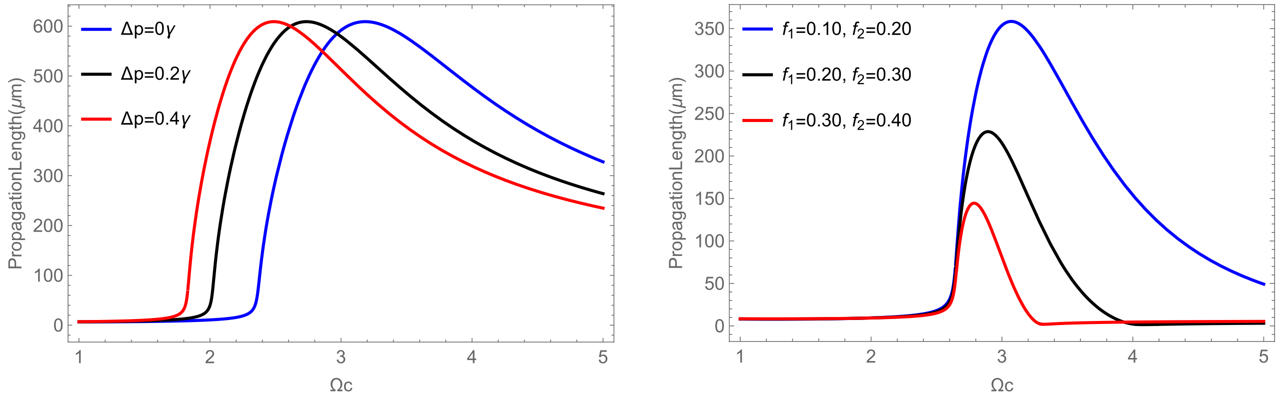

(c) Propagation length versus Ω_c for different values of Δ_p where $\Delta_c = 1\gamma$, $f_1 = 0.10$ and $f_2 = 0.20$ $\gamma_{21} = 0.09\gamma$.

(d) Propagation length versus Ω_c for different values of f_1 and f_2 where $\Delta_c = 1\gamma$ and $\Delta_p = 0$, $\gamma_{21} = 0.09\gamma$.

Figure 4. Propagation length of SPPs.

Figure 6 depicts the reflection and transmission spectra against the control field for different probe detunings and different values of f_1 and f_2. In Fig. 6a,b, we plot reflection and transmission versus Ω_c for different values of Δ_p. We observe peaks (blue, red, and green) that show 95% reflection for three probe detunings (0γ, 0.2γ, 0.4γ) at $\Omega_c = 0.7\gamma$, 0.9γ, and 1.1γ, respectively. Note that beyond probe detuning $\Omega_c = 2\gamma$, the reflection is zero. Similarly, for transmission versus Ω_c, as Δ_p varies, we notice dips (indicating zero transmission) at distinct values of the control field, and from $\Omega_c = 2\gamma$ to 3γ, the transmission is maximized. Figure 6c demonstrates the reflection spectrum for various fraction ratios of metallic components. The reflection peaks exhibit 85%, 95%, and complete reflection for $f_1 = 0.10$, $f_2 = 0.20$; $f_1 = 0.20$, $f_2 = 0.30$; and $f_1 = 0.30$, $f_2 = 0.40$, respectively. Furthermore, for transmission versus Ω_c in Fig. 6d, the blue, red, and green dips reveal minimum transmission, and subsequently, it reaches a maximum for all values of f_1 and f_2 at $\Omega_c = 3\gamma$.

Symmetric and anti-symmetric eigenvalues

The graphs of symmetric ($|S_+|^2$) and anti-symmetric ($|S_-|^2$) eigenvalues are obtained by using Eq. (21). In Fig. 7a, we plot the symmetric and anti-symmetric eigenvalues for various control field strengths and fraction ratios of metallic components of both layers. We observe an interesting and typical behavior of $|S_+|^2$ and $|S_-|^2$. When we increase the value of Ω_c, it leads to strong coupling between probe detuning and different eigenstates of the system, leading to interference; hence, perfect absorption is the result of destructive interference. We observe CPA of symmetric eigenvalues in the negative detuning region ($\Delta_p = -0.8\gamma$ and -1.1γ), as shown by the blue-black sharp dips, while anti-symmetric eigenvalues exhibit up to 97% absorption (see red and green dips on the negative detuning side). From the resonance point to a probe detuning of 0.8γ, symmetric eigenmodes show no absorption, which reaches 50% at $\Delta_p = 1.2\gamma$ and 1.5γ for $\Omega_c = 1\gamma$ and 1.5γ, respectively. Similarly, for $|S_-|^2$ at $\Delta_p = 0.1\gamma$, we observe 95% absorption, which gradually reduces and hence becomes minimal.

Figure 7b depicts symmetric and anti-symmetric eigenvalues versus probe detuning for different values of f_1 and f_2. We detect CPA for anti-symmetric eigenvalues in the negative detuning region, i.e., -0.8γ (green sharp dip) for $f_1 = 0.30$ and $f_2 = 0.40$. In contrast, for symmetric eigenvalues of the scattering matrix, we observe complete absorption for $f_1 = 0.20$ and $f_2 = 0.30$ at a probe detuning of 1.6γ (see blue and black curves).

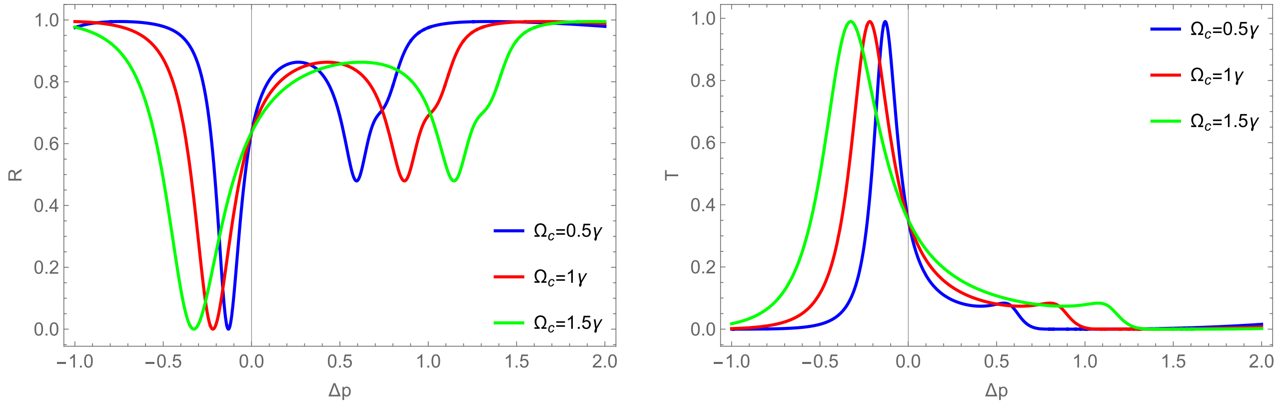

(a) Reflection versus Δ_p for different values of Ω_c where $\Delta_c = 1\gamma$, $f_1 = 0.10$, and $f_2 = 0.20$.

(b) Transmission versus Δ_p for different values of Ω_c where $\Delta_c = 1\gamma$, $f_1 = 0.10$, and $f_2 = 0.20$.

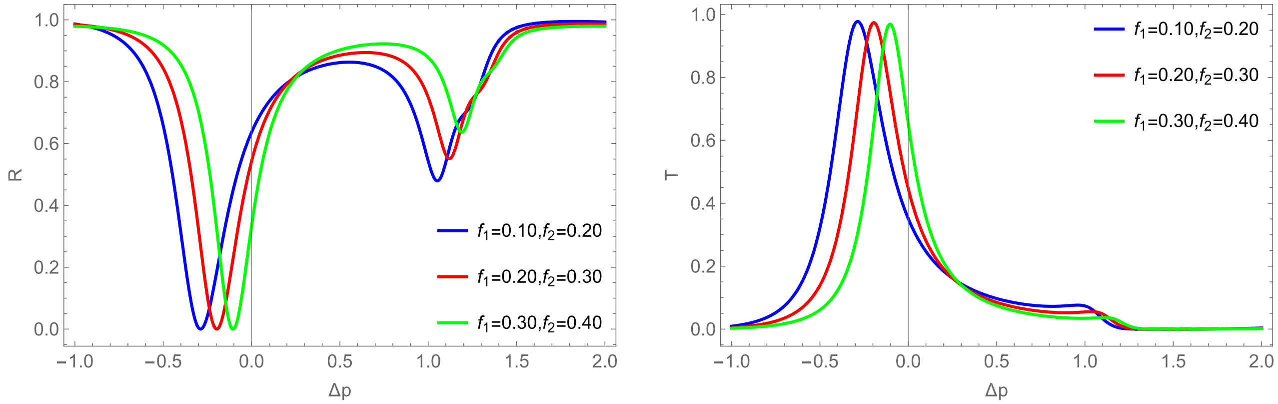

(c) Reflection versus Δ_p for different values of f_1 and f_2 where $\Delta_c = 1\gamma$ and $\Omega_c = 1.5\gamma$.

(d) Transmission versus Δ_p for different values of f_1 and f_2 where $\Delta_c = 1\gamma$ and $\Omega_c = 1.5\gamma$.

Figure 5. Reflection and transmission spectrum of SPPs.

Control field and metal composition ratio influences

The control field modifies the optical permittivity tensor of the uniaxial dielectric through field-induced birefringence (or electro-optic modulation), effectively altering the effective refractive index seen by the SPP mode. This shifts the in-plane wavevector k_x, leading to changes in the SPP dispersion relation and wavelength. As the dielectric environment becomes more anisotropic under higher control field intensity, mode confinement and energy dissipation (absorption) also change accordingly.

Changing the fractional composition of the metallic layers changes the average plasma frequency and damping rate in the system. Since SPP propagation strongly depends on the dielectric function of the metal (through the Drude or Drude–Lorentz model), changes in the composition ratio modulate the loss (imaginary part of permittivity) and confinement (real part), thus directly affecting both the propagation length and absorption profile. This tunability enables engineered resonance conditions that can lead to complete absorption under the right phase and amplitude matching.

Conclusions

We investigated the coherent control of anisotropic SPPs through an identical double-layer metal/uniaxial dielectric interface. Specifically, we considered the dielectric of the first and second layers (ϵ_{1d}, ϵ_{2d}) to contain three-level Λ-type atomic configurations. By employing coherent control, we calculated the reflection and transmission coefficients, the dispersion relation, the wavelength, the propagation length of SPPs, and the symmetric/anti-symmetric eigenvalues of the scattering matrices. The dispersion and absorption spectra of SPPs were enhanced by changing the fractional ratios (f_1, f_2) of the metallic components of both layers. Furthermore, by increasing the fraction ratios of metallic components of both layers (f_1, f_2), the wavelength increased up to 450 nm, and at a control field strength of 0.5γ, we found $\lambda_{\text{sppx}} = 560$ nm. Similarly, by increasing Ω_c, the propagation distance increased, and we obtained $L_{\text{sppx}} = 420\ \mu$m. For probe detuning values of 0γ, 0.2γ, and 0.4γ, we found $L_{\text{sppx}} = 600\ \mu$m.

Moreover, we examined the impact of these parameters on the reflection and transmission spectra of SPPs, and demonstrated how they could be used to enhance transmission while suppressing reflection, and vice versa. Additionally, for $|S_+|^2$ and $|S_-|^2$, we observed CPA at $\Omega_c = 1\gamma$, 1.5γ, and for $f_1 = 0.30$, $f_2 = 0.40$. The coherent control of anisotropic SPPs through an identical double-layer metal/uniaxial dielectric interface served

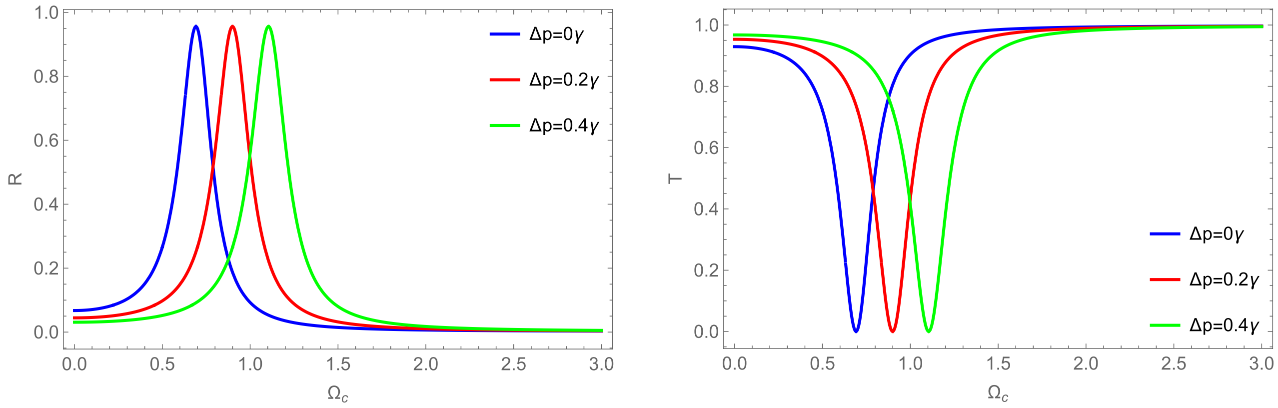

(a) Reflection versus Ω_c for different values of Δ_p where $\Delta_c = 1\gamma$, $f_1 = 0.10$, and $f_2 = 0.20$.

(b) Transmission versus Ω_c for different values of Δ_p where $\Delta_c = 1\gamma$, $f_1 = 0.10$, and $f_2 = 0.20$.

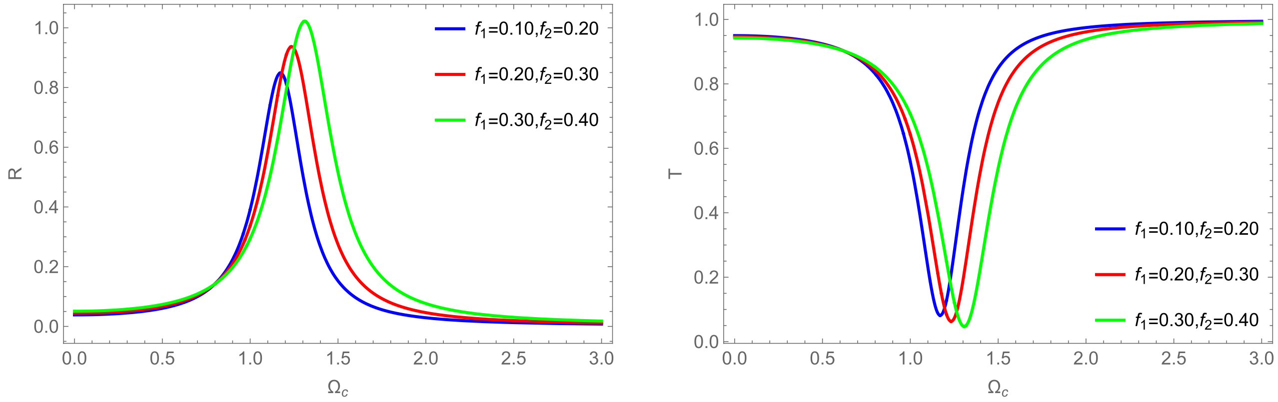

(c) Reflection versus Ω_c for different values of f_1 and f_2 where $\Delta_p = 0\gamma$ and $\Delta_c = 1\gamma$.

(d) Transmission versus Ω_c for different values of f_1 and f_2 where $\Delta_p = 0\gamma$ and $\Delta_c = 1\gamma$.

Figure 6. Reflection and transmission spectrum of SPPs.

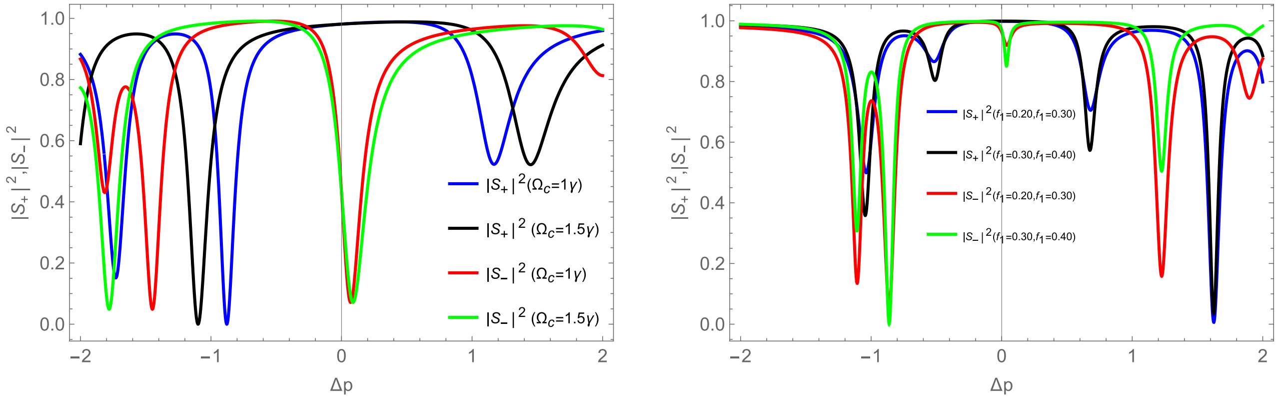

(a) $|S_+|^2$ and $|S_-|^2$ versus Δ_p for different values of Ω_c. Fixed parameters are $\Delta_c = 1\gamma$, $f_1 = 0.10$ and $f_2 = 0.20$.

(b) $|S_+|^2$ and $|S_-|^2$ versus Δ_p for different values of f_1 and f_2. Fixed parameters are $\Omega_c = 1.5\gamma$ and $\Delta_c = 1\gamma$.

Figure 7. Symmetric ($|S_+|^2$) and anti-symmetric ($|S_-|^2$) eigenvalues of scattering matrix.

as a precursor to the fine tuning, accurate control, and confinement of plasmonic modes. Therefore, plasmonic modes became more sensitive, and this control capability enabled the realization of compact, high-performance, and efficient photonic systems. Hence, our results have significant applications in sensing, plasmonics-based logic gates, integrated nanophotonic systems, and waveguiding.

Data availability

All data generated or analyzed during this study are included in this published article.

Received: 8 June 2025; Accepted: 16 July 2025

References

1. Maier, S.A. *Plasmonics: Fundamentals and Applications* vol 1 (Springer, 2007).
2. Shahbazyan, T.V. & Stockman, M.I. *Plasmonics: Theory and Applications* vol 15 (Springer, 2013).
3. Berini, Pierre & De Leon, Israel. Surface plasmon-polariton amplifiers and lasers. *Nat. Photonics* **6**(1), 16–24 (2012).
4. Shrivastav, A. M., Cvelbar, U. & Abdulhalim, I. A comprehensive review on plasmonic-based biosensors used in viral diagnostics. *Commun. Biol.* **4**(1), 70 (2021).
5. Ferry, V. E., Sweatlock, L. A., Pacifici, D. & Atwater, H. A. Plasmonic nanostructure design for efficient light coupling into solar cells. *Nano Lett.* **8**(12), 4391–4397 (2008).
6. Barnes, W. L., Dereux, A. & Ebbesen, T. W. Surface plasmon subwavelength optics. *Nature* **424**(6950), 824–830 (2003).
7. Ghaemi, H. F., Thio, T., Grupp, D. E., Ebbesen, T. W. & Lezec, H. J. Surface plasmons enhance optical transmission through subwavelength holes. *Phys. Rev. B* **58**(11), 6779 (1998).
8. Luo, Y. et al. On-chip hybrid photonic-plasmonic light concentrator for nanofocusing in an integrated silicon photonics platform. *Nano Lett.* **15**(2), 849–856 (2015).
9. Lameirinhas, R. A. M., Torres, J. P. N., Baptista, A. & Martins, M. J. M. A new method to analyse the role of surface plasmon polaritons on dielectric-metal interfaces. *IEEE Photonics J.* **14**(4), 1–9 (2022).
10. Dai, Y. et al. Poincaré engineering of surface plasmon polaritons. *Nature Rev. Phys.* **4**(9), 562–564 (2022).
11. Waheed, M. et al. Surface plasmon polaritons at an interface between silver and quantum dots hybrid nanocomposite. *Phys. Scr.* **97**(10), 105104 (2022).
12. Rahman, H., Ali, H., Ahmad, I., Din, R. U. & Ge, G. Q. Magneto-optical rotation of surface plasmon polaritons. *J. Phys. D Appl. Phys.* **54**(17), 175107 (2021).
13. Rahman, H. et al. Coherent surface plasmon hole burning via spontaneously generated coherence. *Molecules* **26**(21), 6497 (2021).
14. Costa, A. T., Vasilevskiy, M. I., Fernández-Rossier, J. & Peres, N. M. R. Strongly coupled magnon-plasmon polaritons in graphene-two-dimensional ferromagnet heterostructures. *Nano Lett.* **23**(10), 4510–4515 (2023).
15. In, C., Kim, U. J. & Choi, H. Two-dimensional dirac plasmon-polaritons in graphene, 3d topological insulator and hybrid systems. *Light Sci. Appl.* **11**(1), 313 (2022).
16. Evseev, D. A. & Sementsov, D. I. Surface plasmon polaritons at the boundary of a graphene-based thin-layer medium. *Phys. Solid State* **60**, 616–621 (2018).
17. Hua, X., Sun, D., Liu, D. & Ma, N. The double-layer graphene surface plasmon-polaritons spectrum in hydrodynamic model. *Plasmonics* **28**, 1–9 (2024).
18. Bezus, E. A., Doskolovich, L. L. & Kazanskiy, N. L. Low-scattering surface plasmon refraction with isotropic materials. *Opt. Express* **22**(11), 13547–13554 (2014).
19. Chu, M. H. & Trinh, M. T. Enhancing propagation length of surface plasmon polaritons by using metallic double-layer structure. *IEEE Photonics J.* **11**(5), 1–9 (2019).
20. Kotov, O. V. & Lozovik, Yu. E. Hyperbolic hybrid waves and optical topological transitions in few-layer anisotropic metasurfaces. *Phys. Rev. B* **100**, 165424 (2019).
21. Sokolik, A. A., Kotov, O. V. & Lozovik, Y. E. Plasmonic modes at inclined edges of anisotropic two-dimensional materials. *Phys. Rev. B* **103**, 155402 (2021).
22. Liang, Y. et al. Bound states in the continuum in anisotropic plasmonic metasurfaces. *Nano Lett.* **20**(9), 6351–6356 (2020).
23. Liang, Y. et al. Hybrid anisotropic plasmonic metasurfaces with multiple resonances of focused light beams. *Nano Lett.* **21**(20), 8917–8923 (2021).
24. Xing, Q. et al. Tunable anisotropic van der waals films of 2m-ws2 for plasmon canalization. *Nat. Commun.* **15**(1), 2623 (2024).
25. Darinskii, A. N. Surface plasmon polaritons in metal films on anisotropic and bianisotropic substrates. *Phys. Rev. A* **104**(2), 023507 (2021).
26. Ahn, S. & Das Sarma, S. Theory of anisotropic plasmons. *Phys. Rev. B* **103**(4), L041303 (2021).
27. Elston, S.J. & Sambles, J.R. Surface plasmon-polaritons on an anisotropic substrate. (1990).
28. Warmbier, R., Manyali, G. S. & Quandt, A. Surface plasmon polaritons in lossy uniaxial anisotropic materials. *Phys. Rev. B Condens. Matter Mater. Phys.* **85**(8), 085442 (2012).
29. Gric, T. & Rafailov, E. Propagation of surface plasmon polaritons at the interface of metal-free metamaterial with anisotropic semiconductor inclusions. *Optik* **254**, 168678 (2022).
30. Ioannidis, T., Gric, T. & Rafailov, E. Tunable polaritons of spiral nanowire metamaterials. *Waves Random Compl. Media* **32**(1), 381–389 (2020).
31. Evseev, D. A., Sannikov, D. G. & Sementsov, D. I. Surface plasmon polaritons at the interface between dielectric and anisotropic nanocomposite. *J. Commun. Technol. Electron.* **60**, 158–165 (2015).
32. Zhao, R., Liu, X., Zhang, Y. & Li, J. Propagation characteristics of surface plasmon polaritons near anisotropic 2d materials sandwiched by chiral media. *Ann. Phys.* **535**(2), 2200321 (2023).
33. Golenitskii, K. Y. Anisotropic surface polaritons at isotropic-uniaxial interface: An exact algebraic solution. *Phys. Rev. B* **110**(3), 035301 (2024).
34. Liscidini, M. & Sipe, J. E. Quasiguided surface plasmon excitations in anisotropic materials. *Phys. Rev. B* **81**(11), 115335 (2010).
35. Feng, L., Liu, Z., Lomakin, V. & Fainman, Y. Form birefringence metal and its plasmonic anisotropy. *Appl. Phys. Lett.* **96**(4), 124 (2010).
36. Li, X., Gu, Y., Luo, R., Wang, L. & Gong, Q. Effects of dielectric anisotropy on surface plasmon polaritons in three-layer plasmonic nanostructures. *Plasmonics* **8**, 1043–1049 (2013).
37. Ghazali, F. A. M., Fujii, M. & Hayashi, S. Anisotropic propagation of surface plasmon polaritons caused by oriented molecular overlayer. *Appl. Phys. Lett.* **95**(3), 24 (2009).
38. Gazzola, E. Anisotropic propagation of surface plasmon polaritons: study and exploitations. (2014).
39. Rizzo, D.J., Seewald, E., Zhao, F., Cox, J. & Xie, K. Uniaxial plasmon polaritons via charge transfer at the graphene/crsbr interface. *arXiv preprint* arXiv:2407.07178, (2024).
40. Wu, Y., Wu, W. & Dai, X. Spps in a double layer graphene system with an anisotropic dielectric. *Results Phys.* **15**, 102718 (2019).
41. Heydari, M. B. & Samiei, M.H.V. Magneto-plasmons in grounded graphene-based structures with anisotropic cover and substrate. *arXiv preprint* arXiv:2103.08557, (2021).
42. Amanatiadis, S.A., Karamanos, T.D. & Kantartzis, N.V. Surface plasmon polariton waves onto graphene's surface over an anisotropic metamaterial substrate. In *Metamaterials IX* vol. 9125, pp 15–24 (SPIE, 2014).
43. Rodin, A. S. & Castro Neto, A. H. Collective modes in anisotropic double-layer systems. *Phys. Rev. B* **91**(7), 075422 (2015).

44. Inampudi, S., Nazari, M. & Forouzmand, A. Manipulation of surface plasmon polariton propagation on isotropic and anisotropic two-dimensional materials coupled to boron nitride heterostructures. *J. Appl. Phys.* **119**(2), 1457 (2016).
45. Milton, G. W. & Sawicki, A. T. Theory of composites Cambridge monographs on applied and computational mathematics. *Appl. Mech. Rev.* **56**(2), B27–B28 (2003).
46. Podolskiy, V. A. & Elser, J. Scattering-free plasmonic optics with anisotropic metamaterials. *Phys. Rev. Lett.* **100**(6), 066402 (2008).
47. Baldacci, L., Zanotto, S., Biasiol, G., Sorba, L. & Tredicucci, A. Interferometric control of absorption in thin plasmonic metamaterials: General two port theory and broadband operation. *Opt. Express* **23**(7), 9202–9210 (2015).
48. Chong, Y. D., Ge, Li., Cao, Hui & Stone, A Douglas. Coherent perfect absorbers: Time-reversed lasers. *Phys. Rev. Lett.* **105**(5), 053901 (2010).
49. Iqbal, T. Propagation length of surface plasmon polaritons excited by a 1D plasmonic grating. *Curr. Appl. Phys.* **15**(11), 1445–1452 (2015).

Acknowledgements

We are thankful to the Higher Education Commission (HEC) of Pakistan for providing research facilities under NRPU Grant. Ref No. 20-14568/NRPU/RD/HEC/2021.

Author contributions

J.K., A.S., A.R., M.S., H.A., and S.H. have contributed to writing the manuscript and interpreting the results. Thorough checking of the manuscript and confirming the conclusions were done by H.A. and S.H.

Funding

No funding.

Declarations

Competing interests

The authors declare that they have no known competing financial interests.

Additional information

Correspondence and requests for materials should be addressed to H.A. or S.H.